Informatics in Medicine Unlocked 26 (2021) 100709

Contents lists available at ScienceDirect

Informatics in Medicine Unlocked

journal homepage: www.elsevier.com/locate/imu

COVID-19 identification from volumetric chest CT scans using a progressively resized 3D-CNN incorporating segmentation, augmentation, and class-rebalancing

Md. Kamrul Hasan [a,*], Md. Tasnim Jawad [a], Kazi Nasim Imtiaz Hasan [b], Sajal Basak Partha [b], Md. Masum Al Masba [b], Shumit Saha [c], Mohammad Ali Moni [d,e]

[a] Department of Electrical and Electronic Engineering, Khulna University of Engineering & Technology, Khulna-9203, Bangladesh
[b] Department of Computer Science and Engineering, Khulna University of Engineering & Technology, Khulna-9203, Bangladesh
[c] Department of Electronics and Communication Engineering, Khulna University of Engineering & Technology, Khulna-9203, Bangladesh
[d] Department of Computer Science & Engineering, Pabna University of Science and Technology, Pabna-6600, Bangladesh
[e] School of Health and Rehabilitation Sciences, Faculty of Health and Behavioural Sciences, The University of Queensland, St Lucia, QLD 4072, Australia

ARTICLE INFO

Keywords:
COVID-19
3D convolutional neural network
Volumetric chest CT scans
3D patches
Progressive resizing

ABSTRACT

The novel COVID-19 is a global pandemic disease overgrowing worldwide. Computer-aided screening tools with greater sensitivity are imperative for disease diagnosis and prognosis as early as possible. It also can be a helpful tool in triage for testing and clinical supervision of COVID-19 patients. However, designing such an automated tool from non-invasive radiographic images is challenging as many manually annotated datasets are not publicly available yet, which is the essential core requirement of supervised learning schemes. This article proposes a 3D Convolutional Neural Network (CNN)-based classification approach considering both the inter-and intra-slice spatial voxel information. The proposed system is trained end-to-end on the 3D patches from the whole volumetric Computed Tomography (CT) images to enlarge the number of training samples, performing the ablation studies on patch size determination. We integrate progressive resizing, segmentation, augmentations, and class-rebalancing into our 3D network. The segmentation is a critical prerequisite step for COVID-19 diagnosis enabling the classifier to learn prominent lung features while excluding the outer lung regions of the CT scans. We evaluate all the extensive experiments on a publicly available dataset named MosMed, having binary- and multi-class chest CT image partitions. Our experimental results are very encouraging, yielding areas under the Receiver Operating Characteristics (ROC) curve of 0.914 ± 0.049 and 0.893 ± 0.035 for the binary- and multi-class tasks, respectively, applying 5-fold cross-validations. Our method's promising results delegate it as a favorable aiding tool for clinical practitioners and radiologists to assess COVID-19.

1. Introduction

Pneumonia of unknown cause discovered in Wuhan, China, was published to the World Health Organization (WHO) office in China on 31st December 2019. It was consequently assigned to Severe Acute Respiratory Syndrome Coronavirus 2 (SARS-CoV-2) because of having similar genetic properties to the SARS outbreak of 2003. Therefore, on 11th February 2020, WHO termed that new disease as COVID-19 (Coronavirus disease), which displays an upper respiratory tract and lung infection [1]. The clinical characteristics of critical COVID-19 pandemic are bronchopneumonia that affects cough, fever, dyspnea, and detailed respiratory anxiety ailment [2–4]. According to the WHO reports, COVID-19's general indications are equivalent to that of ordinary flu, including fever, tiredness, dry cough, shortness of breath, aches, pains, and sore throat [5]. Those shared signs turn it challenging to recognize the virus at an ancient step. Moreover, the aforementioned is a virus, which works on bacterial or fungal infections [5,6] with no possibility that antibiotics can restrict it. Besides, people suffering from medical complications, like diabetes and chronic respiratory and cardiovascular diseases, can undergo COVID-19. An explanatory statement of the Imperial College advised that the affection rate will be more than

* Correspondence to: Department of EEE, KUET, Khulna-9203, Bangladesh.
E-mail addresses: m.k.hasan@eee.kuet.ac.bd (M.K. Hasan), jawad1703006@stud.kuet.ac.bd (M.T. Jawad), hasan1607097@stud.kuet.ac.bd (K.N.I. Hasan), partha1607101@stud.kuet.ac.bd (S.B. Partha), masba@cse.kuet.ac.bd (M.M.A. Masba), shumit.saha@mail.utoronto.ca (S. Saha), m.moni@uq.edu.au (M.A. Moni).

https://doi.org/10.1016/j.imu.2021.100709
Received 27 June 2021; Received in revised form 11 August 2021; Accepted 18 August 2021
Available online 28 August 2021

90.0% of the world's people, killing 40.6 million people if no reduction actions are grasped to combat the virus [7].

Advanced presumed discovery of COVID-19 is also a challenge for public health security and control of pandemics. The COVID-19 detection failure increases the mortality rate exponentially. The incubation period, which is a time between catching the virus and causing to have indications of the illness, is $1 \sim 14$ days, making it remarkably challenging to identify COVID-19 infection at a preliminary stage of an individual's symptoms [5]. The clinical screening test for the COVID-19 is Reverse Transcription Polymerase Chain Reaction (RT-PCR), practicing respiratory exemplars. However, it is a manual, complicated, tiresome, and time-consuming fashion with an estimated true-positive rate of 63.0% [8]. There is also a significant lack of RT-PCR kit inventory, leading to a delay in preventing and curing coronavirus disease [9]. Furthermore, the RT-PCR kit is estimated to cost around $120 \sim 130$ USD. It also requires a specially designed biosafety laboratory to house the PCR unit, each of which can cost $15,000 \sim 90,000$ USD [10]. Nevertheless, using a costly screening device with delayed test results makes it more challenging to restrict the disease's spread. Inadequate availability of screening workstations and measurement kits constitutes an enormous hardship to identify COVID-19 in this pandemic circumstance. In such a situation, speedy and trustworthy presumed COVID-19 cases are a massive difficulty for related personals.

However, it is observed that most of the COVID-19 incidents have typical properties on radiographic Computed Tomography (CT) and X-ray images, including bilateral, multi-focal, ground-glass opacities with a peripheral or posterior distribution, chiefly in the lower lobes and early- and late-stage pulmonary concentration [11–14]. Those features can be utilized to build a sensitive Computer-aided Diagnosis (CAD) tool to identify COVID-19 pneumonia, which is deemed an automated screening tool [15]. Currently, deep Convolutional Neural Networks (CNNs) allow for building an end-to-end model without requiring manual and time-consuming feature extraction and engineering [16–19], demonstrating tremendous success in many domains of medical imaging, such as arrhythmia detection [20–22], skin lesion segmentation and classification [23–26], breast cancer detection [27–29], brain disease segmentation and classification [30,31], pneumonia detection from chest X-ray images [32], fundus image segmentation [33,34], and lung segmentation [35]. Most recently, various deep CNN-based methods have been published for identifying COVID-19 from X-rays and CT images, summarizing and bestowing in Table 1, where the mixed datasets indicate that data have come from different open-sources. Though the results obtained in the current articles are promising, they exhibit limited scope for use as a CAD tool, as most of the works, especially on x-ray images, have been based on data coming from different sources for two distinct classes (Covid Vs. Normal) [14,75,76,79,84–87]. This brings inherent bias on the algorithms as the model tends to learn the distribution of the data source for binary classification problems [74]. Therefore, these models perform very low when used in practical settings, where the models have to adapt to data from different domains [74]. Recently, the authors in [88] launched a public chest volumetric CT scan dataset with 1110 COVID-19 related studies (see details in Section 2.1). However, the published articles [89,90] on this dataset consider only intra-slice spatial voxel information to isolate COVID-19 and regular healthy patients.

This article aims to evaluate the proposed 3D-CNN classifier's performance for identifying COVID-19 utilizing volumetric chest images, where the volumes have come from the same source (details in Section 2.1). However, the core contributions in this article are enlisted as follows:

- Designing a 3D-CNN-based classification network for volumetric CT images as the 3D networks account for the inter-and intra-slice spatial voxel information while the 2D networks consider only the intra-slice spatial voxel information [83,90–94]
- Conducting 3D patch-based classification as it increases the sample numbers in the smaller datasets, where we perform ablation studies to determine a proper patch size
- Progressively increasing the input patch size of our network up to the original CT size of $R \times C \times S$, where the trained network with the patch size of $(R/2^{n+1}) \times (C/2^{n+1}) \times (S/2^{n+1})$ is a pre-trained model of a network with the patch size of $(R/2^{n}) \times (C/2^{n}) \times (S/2^{n})$
- Developing an unsupervised lung segmentation pipeline for allowing the classifier to learn salient lung features while omitting the outer lung areas of the CT scans
- Class rebalancing and augmentations, such as intensity- and geometry-based, are employed to develop a general network, although a small dataset is being utilized

The remainder of the article is prepared as follows. Section 2 details the materials and methods practiced in the study, including a brief introduction to the methodology and end-to-end 3D-CNN training. Section 3 describes the experimental operations and their corresponding obtained results. Lastly, Section 4 concludes the article.

2. Materials and methods

In this section, we describe the materials utilized and methods to conduct the widespread experiments. We summarize the adopted dataset in the first Section 2.1. The essential integral preprocessing, such as segmentation, augmentation, and class-rebalancing, are reported in the second Section 2.2. The design of the proposed 3D-CNN-based COVID-19 classifier, along with its training protocol, is explained in the third Section 2.3. Finally, in the fourth Section 2.4, we represent used hardware to execute the aimed method and evaluation criterion.

2.1. Dataset

This article's experimentations utilize a publicly usable MosMedData dataset administered by municipal hospitals in Moscow, Russia, from March to April 2020 [88]. This dataset includes anonymized human chest lung CT scans in Neuroimaging Informatics Technology Initiative (NIFTI) format with and without COVID-19 related findings of 1110 studies. The population of MosMedData is distributed as 42% male, 56% female, and 2% others, where the median age of the subjects is 47 years ($18 \sim 97$ years). All the studies ($n = 1110$) are distributed into five following categories, as presented in Table 2. We design two experimental protocols using the MosMedData dataset, such as binary- and multi-class identification, to evaluate our proposed workflow. In binary-class evaluation, we use NOR vs. NCP (Novel COVID-19 Positive), where NCP includes MiNCP-, MoNCP-, SeNCP-, and CrNCP-classes, while in multi-class evaluation, we use NOR vs. MiNCP vs. MoNCP vs. SeNCP. In multi-class protocols, we merge SeNCP- and CrNCP-classes, naming them as SeNCP, as CrNCP has only two samples in the MosMedData dataset. We have applied a 5-fold cross-validation technique to choose training, validation, and testing images as those are not explicitly given by the data provider. The class-wise distribution of the MosMedData dataset in Table 2 illustrates that the class distribution is imbalanced. Such an imbalanced class distribution produces a biased image classifier towards the class having more training samples. Therefore, we apply various rebalancing schemes to develop a generic classifier for COVID-19 identification, even though the dataset is imbalanced.

2.2. Preprocessing

The recommended integral preprocessing in the proposed framework (see in Fig. 1) consists of segmentation, augmentations (both geometry- and intensity-based), and class-rebalancing, which are concisely explained as follows:

Table 1
Numerous published articles for the COVID-19 identification with their respective utilized datasets and performances exhibiting different metrics, such as mSn, mSp, and mF1, respectively, for mean sensitivity (recall), specificity, and F1-score (see metric details in Section 2.4).

Different methods	Datasets	Results
A pre-trained 2D MobileNet-v2 [36] architecture on ImageNet [37] was used to extract massive high-dimensional features to classify six different diseases using the fully-connected layers [38]	Mixed	mSn: 0.974 mSp: 0.994
DeTraC [39,40], where the network was trained first using a gradient descent optimization [41], and then, the class-composition layer of DeTraC was used to refine the final detection results [40]	Mixed	mSn: 0.979 mSp: 0.919
A multi-objective differential evolution-based CNN method fine-tuning iteratively using mutation, crossover, and selection operations to discover the best possible results [14]	Mixed	mSn: 0.907 mSp: 0.906
An ensemble of VGG-16 [42], Inception [43], Xception [44], Inception-ResNet [45], MobileNet [46], DenseNet [47], and NasNet [48] optimizing the hyperparameters using a greedy search algorithm [49,50]	Mixed	mSn: 0.990 mSp: 0.990
Support vector machine [29,51]-based method to classify the in-depth features from the pre-trained MobileNet and SqueezeNet [52] from the restructured the data using a fuzzy color technique [53]	Mixed	mSn: 0.983 mSp: 0.997
An ensemble of three lightweight pre-trained SqueezeNet, ShuffleNet [54], and EfficientNet-B0 [55] at various depths and consolidates feature maps in diverse abstraction levels [56]	Mixed	mSn: 0.978 mSp: 0.985
A fusing and ranking of in-depth features for classifying using a support vector machine, where the pre-trained CNN models on ImageNet were used to extract the COVID-19 features [57]	Mixed	mSn: 0.989 mSp: 0.976
A DenseNet-201 [47]-based transfer learning to extract features using its learned weights on the ImageNet was used to classify the patients as COVID infected or not [58]	[59]	mSn: 0.960 mSp: 0.960
A transfer learning-based approach using one of the VGG, ResNet [60], Inception, or Xception pre-trained deep learning model on ImageNet as a backbone [61]	[62]	mSn: 0.996 mSp: 0.100
A weakly-supervised learning schema, where the lung region was segmented using a pre-trained UNet [63]; then, a 3D network was used to predict the probability of COVID-19 infectious [64]	[64]	mSn: 0.911 mSp: 0.881
A multi-scale-multi-encoder ensemble of CNN model aggregating the outputs from two different encoders and their different scales to obtain the final prediction probability [65]	Mixed	mSn: 0.997 mSp: 0.997
Advanced deep network architectures proposing a transfer learning strategy on ImageNet using a custom-sized input tailored for each architecture to achieve the best possible results [66]	Mixed	mSn: 0.996 mSp: 0.998
A pre-trained CNN-based schema leveraging the strength of multiple texture descriptors and base classifiers at once, where data was re-balanced using resampling algorithms [67]	Mixed	mSn: – mF1: 0.889
A deep ResNet-based transfer learning technique with a top-2 smooth loss function and a cost-sensitive attribute to handle noisy and imbalanced COVID-19 datasets [68]	Mixed	mSn: 0.915 mSp: 0.948
An auxiliary classifier generative adversarial network-based design to generate synthetic images, where the synthetic images produced CNN's enhanced results for the prediction [69]	Mixed	mSn: 0.900 mSp: 0.970
A framework consisting of a CNN-based feature extractor and k-nearest neighbor [70,71], support vector machine, and decision tree [71]-based classifiers using the Bayesian algorithm [72]	Mixed	mSn: 0.894 mSp: 0.998
An architecture based on the deep residual neural network using two parallel levels with different kernel sizes for capturing both local and global features of the inputs images [73]	Mixed	mSn: – mF1: 0.967
A classification architecture combining ResNet and Xception to investigate the challenges and limitations of deep CNN and different datasets for building generic COVID-19 classifiers [74]	Mixed	mSn: 0.976 mSp: –
An average rank pooling, multiple-way augmentation, and deep feature fusion-based CNN and graph CNN was developed to fuse individual image-level features and relation-aware features [75]	[75]	mSn: 0.963 mSp: 0.970
An end-to-end DarkCovidNet architecture [76] based on DarkNet [76] gradually increasing the number of filters, where each convolutional layers were followed by BatchNorm [77] and LeakyReLU [78]	Mixed	mSn: 0.951 mSp: 0.953
A CoroNet model based on pre-trained Xception architecture on ImageNet for automated detection of COVID-19 infection and trained in end-to-end manners [79]	Mixed	mSn: 0.993 mSp: 0.986
Comparative analyses of different pre-trained models considering several important factors such as batch size, learning rate, epoch numbers, and type of optimizers to find the best-suited model [80]	Mixed	mSn: 0.100 mSp: 0.967
A comparative analysis of different CNN models, such as VGG, Resnet, Inception, Xception, Inception-ResNet, DenseNet, and NASNet-Large [81], to decide a proper one for multi-modal image classification minimizing the image quality imbalances in the image samples as a preprocessing [82]	Mixed	mSn: 0.820 mSp: – mF1: 0.820
A pipeline consisting of segmentation and subsequent classification employing both 3D and 2D CNNs, where the promising results for detecting were obtained in the 3D-CNNs than the 2D CNNs [83]	[83]	mSn: 0.891 mSp: 0.911

Segmentation. The segmentation, to separate an image into regions with similar properties such as gray level, color, texture, brightness, and contrast, is the significant element for automated detection pipeline [95]. It is also a fundamental prerequisite for the COVID-19 identification as it extracts the lung region and delivers explanatory information about the shapes, structures, and textures. However, this article proposes an unsupervised Lung Segmentation (LS) technique applying different image processing algorithms, as a massive number of annotated COVID-19 images are not available yet in this pandemic situation. Fig. 2 depicts the pipeline of the proposed LS method. The proposed threshold-based LS's primary step is transforming all the CT volumes to Hounsfield units (HU), as it is a quantitative measure of radiodensity for CT scans. We set the HU unit as -1000 to −400 as the study shows that lung regions are within that range, which was also used in many articles [96–98]. The thresholded binary lung masks are then refined to exclude different false-positive regions, such as the connected blobs with the image border and other small false-positive areas and false-negative areas, such as small holes in the lung regions. Firstly, the border-connected regions are eradicated. Secondly, the two largest areas are picked using the region properties algorithm [99]. Thirdly, morphological erosion separates the lung nodules attached to the blood vessels and morphological closing to keep nodules attached to the lung wall. Finally, the false-negative regions are removed using binary hole fill algorithms [100]. Such an unsupervised thresholding-based segmentation method is better for efficiency, taking only a few seconds, and yields utterly reproducible LS.

Table 2
Distribution of utilized MosMedData dataset for COVID-19 identification with a short class description.

Class acronym	Description	PPI*	Samples (%)
NOR	Not consistent with pneumonia, including COVID-19, and refer to a specialist	–	254 (22.8%)
MiNCP	Mild novel COVID-19 positive with ground-glass opacities and follow-up at home using mandatory telemonitoring	=< 25%	684 (61.6%)
MoNCP	Moderate novel COVID-19 positive with ground-glass opacities and follow-up at home by a primary care physician	25 – 50%	125 (11.3%)
SeNCP	Severe novel COVID-19 positive with ground-glass opacities and immediate admission to a COVID specialized hospital	50 – 75%	45 (4.1%)
CrNCP	Critical novel COVID-19 positive with diffuse ground-glass opacities and emergency medical care	>= 75%	2 (0.2%)
Total Samples (%)			1110 (100%)

PPI*: Pulmonary parenchymal involvement.

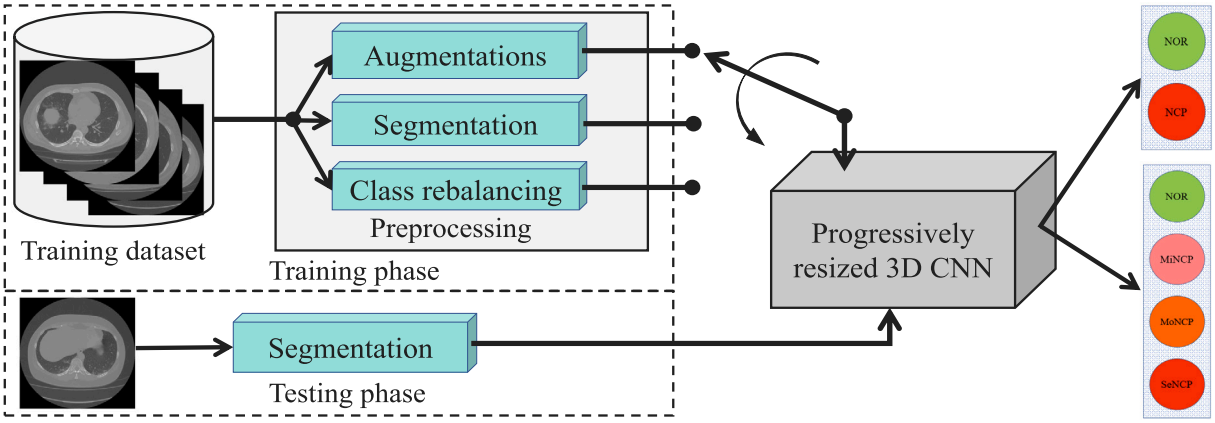

Fig. 1. The intended framework for the automatic COVID-19 identification from the volumetric 3D CT scans, consisting of essential integral preprocessing.

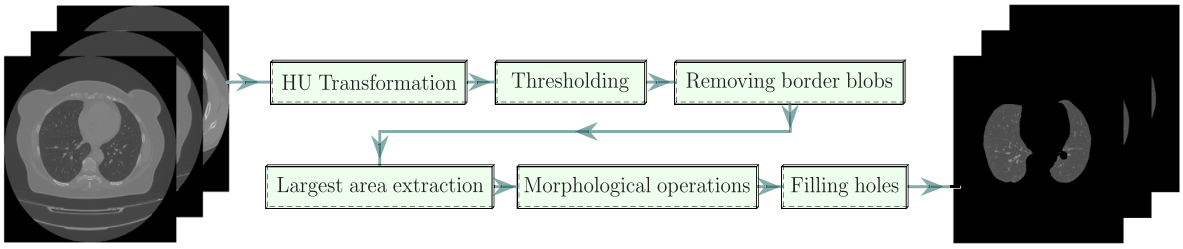

Fig. 2. The proposed block diagram of an unsupervised lung segmentation pipeline, without requiring a manually annotated lung region.

Augmentation. The CNN-based classifiers are profoundly dependent on large data samples to evade the overfitting. Lamentably, various medical imaging fields, especially the current COVID-19 pandemic, suffer from an inadequate dataset size as manually annotated massive training samples are still unavailable. In such a scenario, the augmentations are very dormant preprocessing for increasing the training samples as they are incredibly discriminative [101]. Data augmentation incorporates a method that magnifies training datasets' size and property to develop a better-CNN classifier [102]. The geometric-based augmentation, including a rotation (around $row/2$ and $col/2$) of $-25°$, $-15°$, $10°$, $30°$ and height & width flipping, the intensity-based augmentation, including gamma correction & adding Gaussian random noise, and Elastic deformation[1] are applied in this article as a part of the recommended preprocessing. Two values of gamma (γ), such as 0.7 and 1.7, have been used in gamma correction to adjust the luminance of the CT volumes by $V_{out} = V_{in}^{\gamma}$, where V_{out} and V_{in} individually denote the output and input values of the luminance.

Rebalancing. The utilized dataset in Table 2 is imbalanced. This situation is obvious in the medical diagnosis field due to the scarcity of massive manually annotated training samples, especially in COVID-19 datasets. The undesired class-biasing occurs in the supervised learning systems towards the class with majority samples. However, we apply two techniques to rebalance the imbalanced class distribution, such as adding extra CT volumes (90 samples) from the publicly available CC-CCII dataset (see details in [103]) and weighting the loss function for penalizing the overrepresented class. The latter approach rewards more extra consideration to the class with minority samples. Here, we estimate the class weight using a portion of $W_n = N_n/N$, where W_n, N, and N_n separately denote the nth-class weight, the total sample numbers, and the samples in nth-class. We employ both the class-rebalancing strategies in the binary-class protocol, whereas the only class weighting method is adopted in the multi-class protocol.

[1] https://pypi.org/project/elasticdeform/.

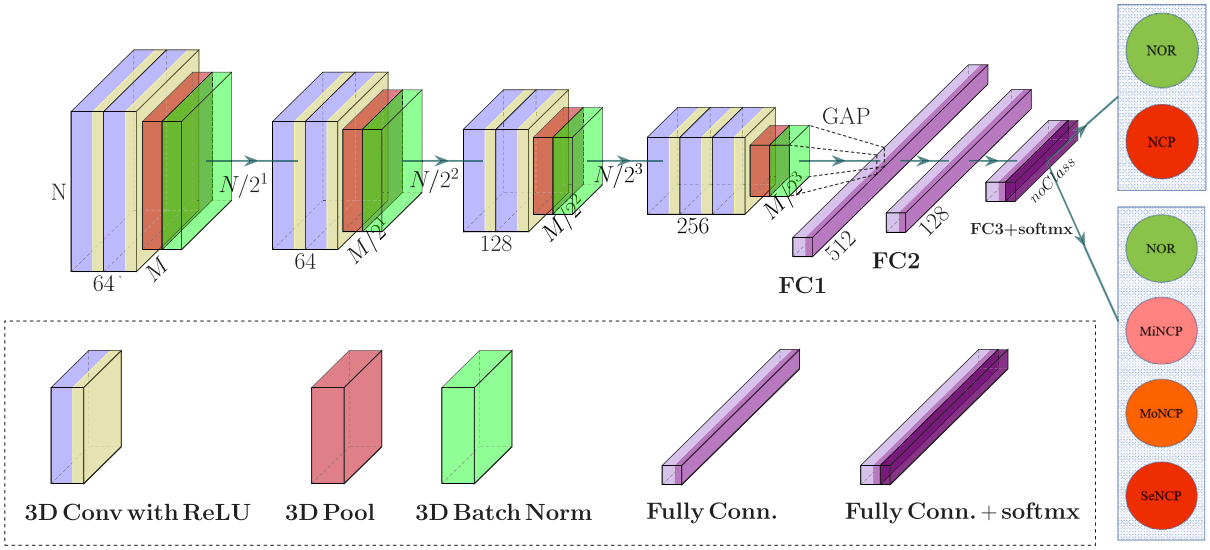

Fig. 3. The architectural construction of the proposed base network, inputted with a size of $M \times N$, training with the most smaller 3D patches. This trained base network is applied as a pre-trained model for the following bigger patches. Best view in the color figure. (For interpretation of the references to color in this figure legend, the reader is referred to the web version of this article.)

2.3. Methodologies

2.3.1. Architecture

The deep neural network is a machine learning framework with a wide range of applications, from natural language processing [104] to medical image classification [105], segmentation [105], and registration [106]. In special, CNNs have become a prevalent technique in the computer vision community. They are practiced in diverse tasks, including object detection [107], classification [108], and localization [109]. The CNN-based deep neural systems are also popularly adopted in recent pandemic for COVID-19 identification [110,111] (see in Table 1). CNN is an excellent discriminant feature extractor at various abstraction levels, which is translation-invariant. Consequently, utilizing it to classify medical images evades complicated and expensive feature engineering [112]. The early few CNN layers learn low-level image features and later layers learn high-level image features particular to the application types [91]. However, the 2D-CNNs are frequently employed in natural RGB and grayscale images to extract the spatial features only in two dimensions [43]. The 2D-CNN also can be applied to the volumetric medical image datasets taking cross-sectional 2D slices of the CT, MRI, or similar scans. However, the recent experimental results have revealed the advantages of 3D-CNN over 2D-CNN, where the 3D-CNN accepts the volumetric spatial information as an input [113]. Conventional 2D-CNNs' effectiveness is degraded due to the loss of spatial voxel information for volumetric 3D medical imaging tasks. A 3D-CNN, a 3D space implementation of convolution and pooling operation, is practiced to overcome spatial voxel information loss as in the 2D-CNNs. The image becomes scalable in the spatial direction using a 3D-CNN, allowing accurate image detection with different frame sizes [114]. Therefore, we propose a classifier based on 3D-CNN to identify COVID-19 from the volumetric CT scans.

Fig. 3 represents the constructional structure of our proposed COVID-19 base classifier of the proposed framework in Fig. 1. The proposed base network in Fig. 3 essentially consists of two modules, such as feature extractor and feature classifier. The former module is a stack of convolutional, pooling, and batch normalization layers, whereas the latter module is a stack of fully connected layers followed by a softmax layer. In addition, we involve 3D layers for all the feature extractor module components to operate on volumetric medical images for extracting the most discriminating features, accounting for both the intra- and inter-slice spatial voxel information. In our network, each 3D convolutional layer with Rectified Linear Unit (ReLU) activation is followed by a 3D max-pooling layer, where the pooling layer increases translational invariances of the network. The pooled feature maps are then used as an input to the successive layers, which may dynamically change during training at each training epoch [92]. The more enormous changes prone to bring difficulties for searching an optimal parameter or hyperparameter; often become computationally expensive to reach an optimal value [77]. Such a problem is mitigated by integrating batch normalization layers in our network [77]. It also facilitates the smooth training of the network architectures in fewer times [92]. The Global Average Pooling (GAP) [115] is used as a bridge layer between the feature extractor and feature classifier modules, converting the feature tensor into a single long continuous linear vector. In GAP, only one feature map is produced for each corresponding category, achieving a more extreme dimensionality compression to evade overfitting [115]. A dropout layer [116] is also employed as a regularizer, which randomly sets half of the activation of the fully-connected layers to zero through the training of our network.

Again, as mentioned earlier, the CNNs are heavily reliant on the massive dataset to bypass overfitting and build a generic network. The acquisition of annotated medical images is arduous to accumulate, as the medical data collection and labeling are confronted with data privacy, requiring time-consuming expert explanations [117]. There are two general resolving directions: accumulating more data, such as crowdsourcing [118] or digging into the present clinical reports [119]. Another technique is investigating how to enhance the achievement of the CNNs with small datasets, which is exceptionally significant because the understanding achieved from the research can migrate the data insufficiency in the medical imaging fields [117]. Transfer learning is a widely adopted method for advancing the performance of CNNs with inadequate datasets [120]. There is no public pre-trained 3D-CNN model for the COVID-19 identification from the volumetric chest images with limited samples to our most trustworthy knowledge. Therefore, we create a pre-trained model by training our base model (see in Fig. 3) on the extracted 3D patches from whole chest CT scans (see details in Section 2.3.2). Then, we double the patches' size and use them for training the modified base network, where we also double the base model's input size applying a stack of convolutional, pooling, and batch normalization layers (see details in Fig. 4). At the same

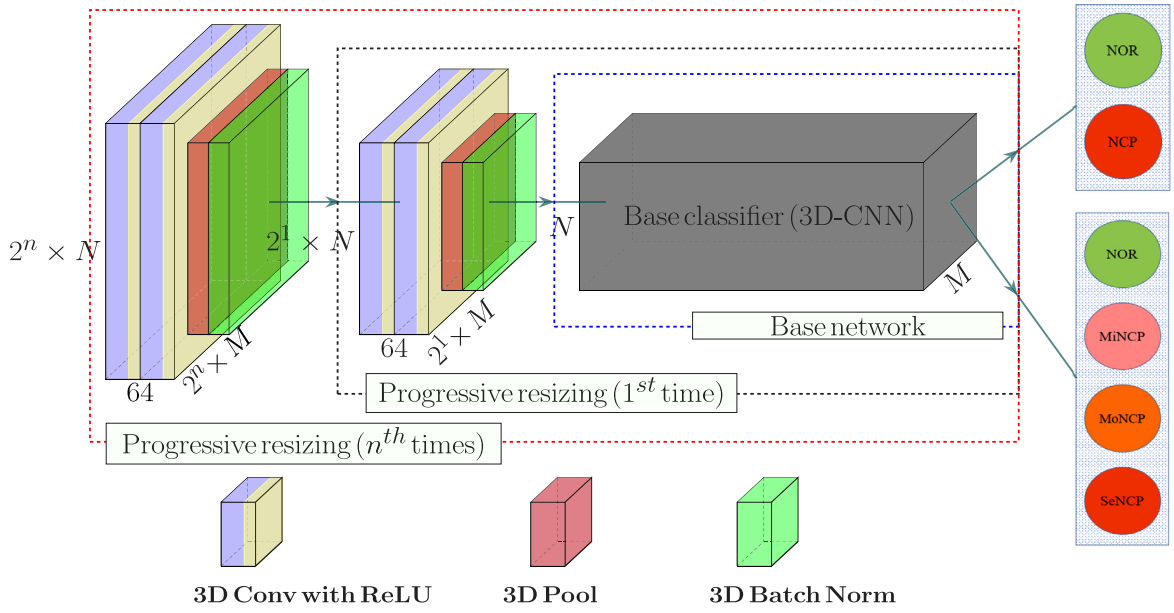

Fig. 4. The proposed progressively resized network's architectural structure, where the base model (see in Fig. 3), inputted with a size of $M \times N$, is trained with the smaller 3D patches. Then, the input size is doubled than the base network's size, termed as 1st-time progressive resizing, where the network trained with the smaller patches is the pre-trained model for the subsequent bigger patches. This process is continued until we reach the original given CT scan size. Best view in the color figure. (For interpretation of the references to color in this figure legend, the reader is referred to the web version of this article.)

time, we keep the base model's trained weights for the smaller patches. We repeat to enlarge (nth-times) the patch and network sizes until we arrive at the provided CT scans' size, as pictured in Fig. 4. Such training is called progressive resizing [121], where the training begins with smaller image sizes followed by a progressive expansion of size. This training process continues until the last patch, and network sizes are the same as the initial image dimension.

2.3.2. Training protocol

We first extract five different patches with different sizes (see in Fig. 5) to begin the experimentations. We perform ablation studies in Section 3.1 looking for the best patch size. The weights of the base network in Fig. 3 are initialized with Xavier's normal distribution. The weights of the first progressively resized network are initialized with the weights of the base network. In general, the weights of the network with the patch size of $(R/2^n) \times (C/2^n) \times (S/2^n)$ are initialized with the weights of the network with the patch size of $(R/2^{n+1}) \times (C/2^{n+1}) \times (S/2^{n+1})$ for the original CT volume size of $R \times C \times S$.

The filters in each layer of the network are initialized with the "he normal" distribution. Categorical cross-entropy and accuracy are utilized as a loss function and metric, respectively, for training all the networks in this article. We use Adam [122] optimizer with initial learning rate (LR), exponential decay rates (β_1, β_2) as $LR = 0.0001$, $\beta_1 = 0.9$, and $\beta_2 = 0.999$, respectively, without AMSGrad [123] variant. The exponential decaying LR schedule is also employed for the networks' optimization. Initial epochs are set as 200, and training is terminated if validation performance stops growing after 15 epochs.

2.4. Hardware and evaluation criterion

We execute all the comprehensive experiments on a *Windows*-10 machine utilizing the Python, with various Keras [124] and image processing APIs, and MATLAB programming languages. The former Python language is utilized to implement a deep learning framework, and the latter MATLAB language is used to access the NIfTI Tool[2] for volumetric medical images. The device configurations of the used machine are: Intel® Core™ i7-7700 HQ CPU @ 3.60 GHz processor with a install memory (RAM) of 32.0 GB, and GeForce GTX 1080 GPU with a memory of 8.0 GB (GDDR5).

We evaluate all the experimental outcomes by employing numerous metrics, such as recall, precision, and F1-score, for evaluating them from diverse perspectives. The mathematical formulations of those metrics are provided in Eq. (1).

$$\begin{aligned} Recall &= \frac{TP}{TP+FN}, \\ Precision &= \frac{TP}{TP+FP}, \\ F1-score &= \frac{2\times TP}{2\times TP+FP+FN}, \end{aligned} \tag{1}$$

where TP, FP, and FN indicate true positive, false positive, and false negative of the detection, respectively. The recall measures the type-II error (the patient having positive COVID-19 characteristics erroneously abandons to be repealed). In contrast, the precision estimates the positive predictive values (a portion of absolutely positive-identification amid all the positive-identification). The harmonic mean of recall and precision is manifested using the F1-score, conferring the trade-off between these two metrics. Furthermore, we also quantify the prognostication probability of an anonymously picked CT sample using a Receiver Operating Characteristics (ROC) with its Area Under the ROC Curve (AUC) value.

3. Results and discussion

In this section, the achieved results from different experiments are reported with a comprehensive discussion. In Section 3.1, we confer the results of COVID-19 identification utilizing various 3D patches and compare them with original CT image utilization on the same experimental conditions and network. We discuss the results of progressive resizing over a single fixed size in Section 3.2. We demonstrate the effects of different proposed preprocessing on COVID-19 identification in Section 3.3. In this subsection, we also investigate a statistical ANOVA test to validate the proposed preprocessing for the aimed task. Finally, in Section 3.4, we dispense the results for binary- and multi-class COVID-19 classification applying our proposed network and preprocessing.

[2] https://in.mathworks.com/matlabcentral/profile/authors/757722.

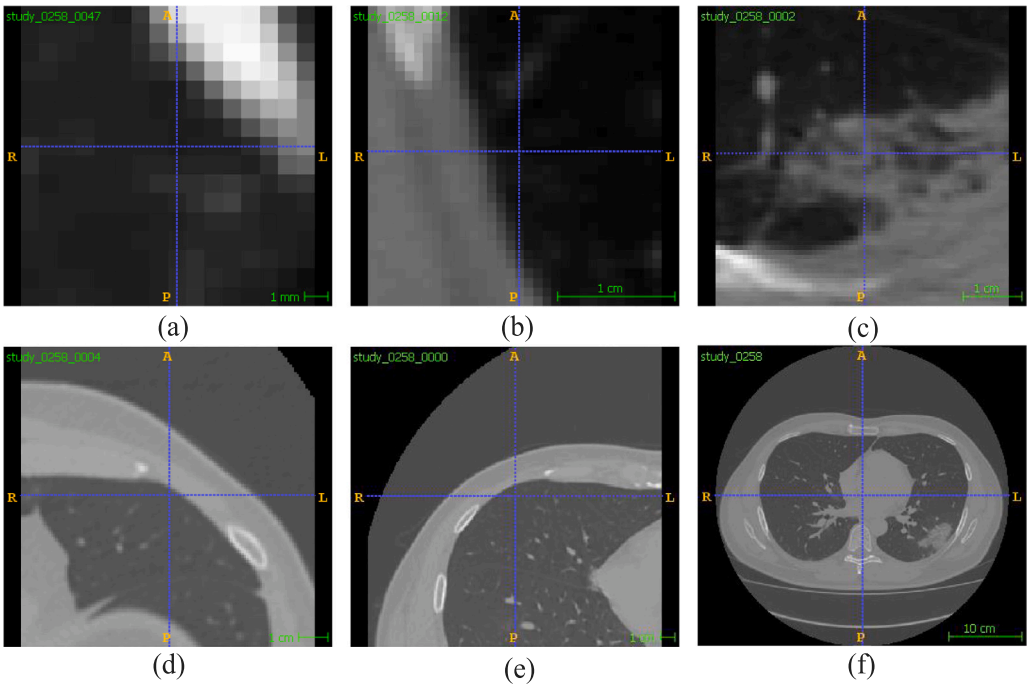

Fig. 5. Example of various extracted patches having different sizes, as mentioned earlier, where patches P_1 to P_6 are displayed in a) to f), respectively. The middle slices of each 3D patches are illustrated for the same sample (*study_0258.nii.gz*) in the MosMedData dataset. Slices are captured using a ITK-Snap windows version.

3.1. Patch selection

We extract five different 3D patches, named P_1, P_2, P_3, P_4, and P_5, having respective size of 16 × 16 × 9, 32 × 32 × 12, 64 × 64 × 15, 128 × 128 × 20, and 256 × 256 × 27. The original CT scans having size of 512 × 512 × 36 is named as P_6. The height and width of the patch P_5 is half of the P_6, whereas these dimensions of the patch P_4 is one-fourth of the P_6, and so on. We extract 2^n number of patches for a nth-time reduction of the height and width. Therefore, we train and test our network with 71040 (= 2^6 × 1110), 35520 (= 2^5 × 1110), 17760 (= 2^4 × 1110), 8880 (= 2^3 × 1110), 4440 (= 2^2 × 1110), and 1110 samples for the 3D volumes P_1 to P_6, respectively. The examples of the extracted patches are shown in Fig. 5, where we select the middle slices of the extracted patches of the same CT scan.

Various patches in Fig. 5 confers their respective resolutions, where it is seen that the patches P_1 and P_2 demonstrate very low resolutions, which may degrade the network's learning capability. However, the effects of those patch resolutions are judged by classifying the NOR vs. NCP classes (see class details in Section 2.1).

The classification results are presented in Fig. 6 for all the patches (P_1 to P_5) and original CT scans (P_6), employing our 3D network without any type of preprocessing. The results determine that the network inputting with P_1 patch outputs COVID-19 identification with type-II errors as 69.0% and 25.0% for NOR- and NCP-classes, respectively. Such results confirm that NCP-class has been identified more accurately (44.0% more in NCP-class), pointing that classifier is biased towards the NCP-class. On the other hand, the utilization of patch P_2 produces identification results with type-II errors as 56.0% and 39.0% for NOR- and NCP-classes, which reduce the differences between these two classes (only 17.0% more in NCP-class). Although the P_1 patch has double samples, it fails to provide a class-balanced performance as in the P_2 patch. This is because of having a better resolution in the P_2 patch than the P_1 patch (see in Fig. 5), as other experimental settings are maintained constant. Those results on P_1 and P_2 patches reveal that significantly less resolution diminishes the CNN's performance, as there is a possibility of losing shape and texture information from the images with meager resolution. Again, the patch P_3 further improves the identification results with type-II errors as 54.0% and 28.0% for NOR- and NCP-classes. Approximately, the patch P_4 also provides similar results to the P_3 patch. It is noteworthy from those experimentations that P_3 or P_4 patches have much fewer samples than P_1 (4-times and 8-times, respectively); still, they outperform the identification results of P_1 and P_2 patches with the same experimental settings. Furthermore, the utilization of patch P_5 further reduces the performances (type-II errors as 6.0% and 99.0% for NOR- and NCP-classes) than all the previous patches discussed above. Such a result explains that it produces a more biased model towards the NCP class. Fig. 5 shows that the patch P_4 and P_5 are visually looking similar but P_4 has two-times samples as of P_5. This experiment exposes that having fewer samples also generates class-biased classifiers if input images are similar in resolution.

Finally, the network with the original images also provides less COVID-19 identification performance as in the patch P_5 (see in Fig. 6). All the experiments illustrate that our network with P_3 or P_4 patches has better identification results. Such experimental results unquestionably prove that the input resolution and the number of samples play an important role in CNN-based classifiers' learning. Unfortunately, we cannot increase the number of specimens taking the smaller patch sizes of the given images in the patch-based strategies, as it has a shallow resolution, which adversely affects the classifiers.

3.2. Progressive resizing

The aforementioned results reveal that the utilization of better-resolution with more sample numbers increases the performance of CNN for image identification. Therefore, we propose to employ progressive resizing of our proposed 3D-CNN (see details in Section 2.3). Firstly, we begin training the recommended network with a suitable 3D patch with more training samples from the previous experiments, acting as a base model. Then, we add some CNN layers to the input of the base model with the higher resolution (2-times more in this article), where the base model is adopted as a pre-trained model (see details in Section 2.3). Finally, we repeat this network resizing until we reach to original given CT size (P_6).

The results for such a progressive resizing are presented in the confusion metrics in Table 3 and ROC curves (with respective AUC

Table 3
Normalized confusion matrix employing our network with progressive resizing, where we progressively increase the input resolution from P_4 to P_5 then to P_6 (original resolution). The first table (left) for the resolution of P_4, the second table (middle) for resolution of $P_4 \longmapsto P_5$, and the last (right) for resolution of $P_4 \longmapsto P_5 \longmapsto P_6$.

P_4		Actual	
		NOR	NCP
Predict	NOR	24.26 %	13.52 %
	NCP	75.74 %	86.48 %

$P_4 \longmapsto P_5$		Actual	
		NOR	NCP
Predict	NOR	21.08 %	5.38 %
	NCP	78.92 %	94.62 %

$P_4 \longmapsto P_5$ $P_5 \longmapsto P_6$		Actual	
		NOR	NCP
Predict	NOR	39.22 %	9.30 %
	NCP	60.78 %	90.70 %

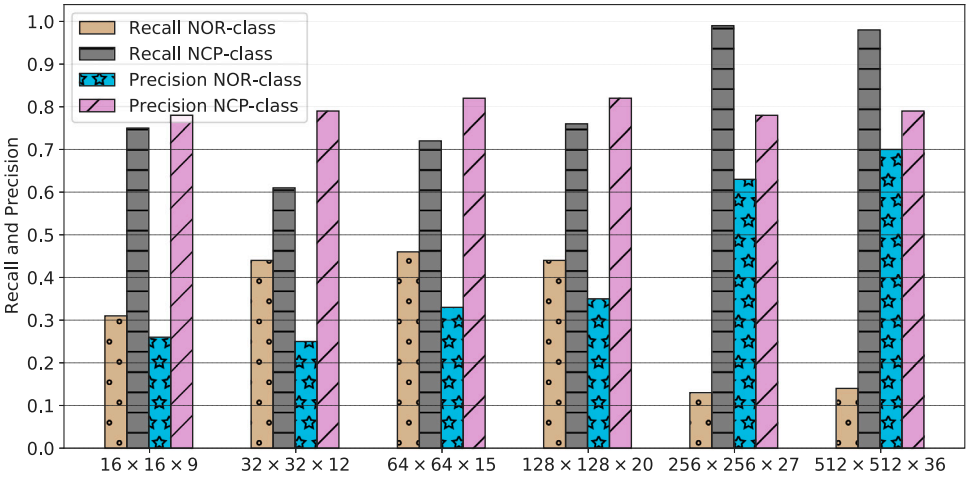

Fig. 6. The binary classification results from our 3D-CNN utilizing different 3D-patch sizes, where the bars with dots, horizontal lines, stars, and diagonal hatching respectively denote recall and precision of NOR- and NCP-classes. Best view in the color figure. (For interpretation of the references to color in this figure legend, the reader is referred to the web version of this article.)

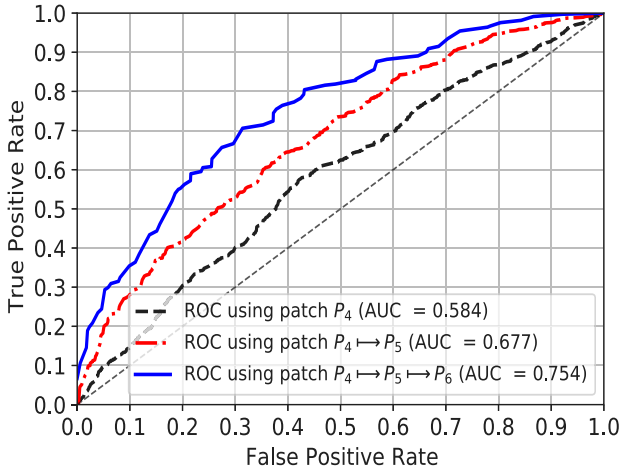

Fig. 7. The ROC curves for the progressive resizing of our 3D network. Best view in the color figure. (For interpretation of the references to color in this figure legend, the reader is referred to the web version of this article.)

values) in Fig. 7. The confusion matrix in Table 3, for more detailed analysis of the identification results, points that 24.26%-NOR samples are accurately classified as NOR, whereas 86.48%-NCP samples are correctly classified as NCP while utilizing the 3D patch P_4 with 8880 samples. Therefore, this training is set as a base model. Now, employing the base model as a pre-trained model, the utilization of P_5 patch, with 4440 samples, decreases the false-negative rate of NCP by 8.14% although false-positive rate increases by 3.18% (see in Table 3 (left and middle)). This training is a first-time progressive resizing ($P_4 \longmapsto P_5$). Again, employing $P_4 \longmapsto P_5$ as a pre-trained model, the utilization of P_6 (original CT scans), with 1110 samples, increases the false-negative rate of NCP by 3.92%, still less than baseline false-negative rate of 13.52%. It also decreases the false-positive rate by a margin of 18.14%, which is less than the former two false-positive rates (see all tables in Table 3). Furthermore, the proposed final progressively resized network ($P_4 \longmapsto P_5 \longmapsto P_6$) obtains an AUC of 0.754, which indicates that the probability of correct COVID-19 identification is as high as 75.4% for any given random CT samples (see in Fig. 7). It has beaten the baseline P_4 and $P_4 \longmapsto P_5$ respectively by 17.0% and 7.70% in terms of AUC, as presented in Fig. 7. Those ROC curves in Fig. 7 also depict that for a given false-positive rate, the possibility of getting a true-positive rate is significantly higher for the $P_4 \longmapsto P_5 \longmapsto P_6$ than the other two approaches. Although the final progressively resized network ($P_4 \longmapsto P_5 \longmapsto P_6$) has an input of the original CT scans, its performance is considerably better than the network training with P_6 alone (see in Fig. 6). Transferring the knowledge from the prior smaller patch inputted network is responsible for achieving much better results than the random initialization of the filter kernels of the proposed network. All the above discussions of this subsection experimentally certify the progressive resizing supremacy for the COVID-19 identification instead of training using single-size input CT scans.

3.3. Prepossessing employment

This subsection exhibits the COVID-19 identification results from our progressively resized 3D network, employing different preprocessing for the ablation studies, such as augmentation, segmentation, and class-rebalancing. At the end of this subsection, the effectiveness of the introduced preprocessing has been validated by applying a statistical ANOVA test.

Table 4 bestows different experimental results, where we explicitly illustrate the outcomes of each preprocessing for the COVID-19 identification from volumetric chest CT scans. Without progressive resizing and inputting with original CT scans (P_6), the baseline model produces low identification consequences resulting in type-II errors of 86.3% and 1.7% respectively for NOR- and NCP-classes, conferring high class-imbalanced results. The weighted average type-II error is only 21.1% with respective average positive predictive value as 77.2%.

Table 4
The COVID-19 identification results on the MosMedData dataset from our 3D-CNN network, utilizing various recommended preprocessing.

Different experiments	Class-wise and weighted average metrics					
	Recall			Precision		
	NOR	NCP	Avg.	NOR	NCP	Avg.
Baseline model	0.137	0.983	0.789	0.700	0.793	0.772
Progressively Resized Network (PRN)	0.392	0.907	0.789	0.556	0.834	0.770
PRN with Augmentation (PRNA)	0.529	0.884	0.803	0.574	0.864	0.798
PRN with Lung Segmentation (PRNS)	0.333	0.971	0.825	0.773	0.831	0.818
PRNA and PRNS with Class-rebalancing (PRNASCR)	0.706	0.919	0.870	0.720	0.913	0.869

The experimental results determine that, on average, 77.2% samples are correctly recognized as positive out of all positive identifications, which are 70.0% and 79.3% for the NOR- and NCP-classes, respectively. Highly imbalanced training samples ($NOR : NCP = 1 : 3.37$) with less intra-class heterogeneity and high inter-class similarity are the probable causes for providing such a poor result of the intended task. However, the utilization of different 3D patches in the following experiment of progressive resizing (PRN) improves the classification results, where the base model on the smaller patches acts as a pre-trained model. This PRN also mitigates the class-imbalanced outcomes, as reflected in the PRN results (see in the second row of Table 4). The appliance of PRN successfully improves the type-II error of NOR-class by a margin of 25.5%, while the weighted average type-II error is identical to the baseline experiment (21.1%). In the PRN, the network is trained with more sample numbers and better resolution (discussed in Section 3.1 and Section 3.2), which improves intra-class heterogeneity and inter-class similarity, leading to enhanced outcomes in the PRN experiment. However, the following three paragraphs explain the results of our progressively resized 3D network, combining Augmentation, Segmentation, and Class-rebalancing in the manner of ablation studies.

PRN with Augmentation (PRNA). The employment of different image augmentations, such as random rotation, height & width flipping, gamma correction, adding Gaussian noise, and Elastic deformation (see details in Section 2.2) with PRN further improves the COVID-19 identification results (see in Table 4). An example of such augmentations is displayed in Fig. 8. It gives far better class-balanced (type-II error of NOR-class improved by a margin of 13.7% with significantly less reduction as 2.3% in NCP-class). The weighted average type-II error is increased by 1.4% with respective increases in average positive predictive value by 2.8% for the appliance of augmentations with the PRN. This experiment reveals that the augmentations bring variability in the training sample with high intra-class heterogeneity and less inter-class similarity, which empowers the CNN model to learn from many examples, driving to enhanced classification results.

PRN with Segmentation (PRNS). The well-defined segmentation, with less coarseness, is an essential requirement for further classification. The incorporation of segmentation with the PRN further promotes the identification results than the PRN alone, as exposed in Table 4. Several examples of the segmented lung from our proposed unsupervised pipeline (as described in Section 2.2) are depicted in Fig. 9 for qualitative evaluation. Those segmentation results quantitatively demonstrate that the segmented lung regions are pretty much accurate visually. However, the COVID-19 identification results incorporating lung segmentation with the PRN reflects its supremacy over the PRN alone, extending the weighted average type-II error by 3.6% with respective improvements in average positive predictive value by 4.8% (see in Table 4). Those results indicate that 4.8% additional specimens are perfectly identified as positive out of all positive classifications. The class-imbalanced identification is also lessened due to segmented lung area utilization over the complete CT volumes. The reasonable ground for those enhanced performances due to the segmentation is that it extracts an abstract region, enabling the classifier to learn only the precise lung areas' features while avoiding the surrounding healthy tissues of the chest CT scans.

PRN with Augmentation, Segmentation, and Class-rebalancing (PRNASCR). Combining augmentations, segmentation, and class-rebalancing with the PRN provides this article's best COVID-19 identification results. This experiment identifies the COVID-19 from the chest CT scans with relatively more minor class imbalance with the weighted average type-II error of 13.0% with respective average positive predictive value as 13.1%. All the preprocessing employment heightens the former metric by a margins of 8.1% and the latter metric by 9.7% from the baseline model (see in Table 4) with less class-imbalance performance. Besides, Fig. 10 displays the ROC curves of our PRN with/without all the preprocessing and a baseline model with their corresponding AUC values. The proposed PRNASCR achieves an AUC of 0.897, determining the probability of accurate COVID-19 recognition is as large as 89.7% for any yielded random chest CT sample. For AUC, the proposed PRNASCR betters the baseline model, PRN, PRNA, and PRNS respectively by 18.9%, 14.3%, 10.9%, and 7.3%. From Fig. 10 and given 10.0% false-positive rates, the true-positive rates of COVID-19 identification from the baseline model, PRN, PRNA, PRNS, and PRNASCR are approximately 22.0%, 35.0%, 46.0%, 52.0%, and 67.0%, respectively, showing the improvements of 45.0% from the baseline 22.0%.

Moreover, the experimental results from different experiments, such as baseline model, PRN, PRNA, PRNS, and PRNASCR, have been confirmed employing a statistical test called ANOVA and 5-fold cross-validation. Fig. 11 dispenses the Box and Whisker plot of the AUC values of this validation test. For ANOVA testing, $\alpha = 0.05$ is applied as a threshold to reject the Null hypothesis (all experiments' mean AUC values are equal) if p-value ≤ 0.05, which outcomes significant results. The ANOVA test demonstrates a p-value of 0.000837 (≤ 0.05), which reveals that an alternative hypothesis is accepted, strongly pointing that none of the mean AUCs are equal (also displayed in Fig. 11). Again, a post hoc T-test (Bonferroni correction) is combined with the ANOVA test for determining the better experiment for the recommended COVID-19 detection system, which confirms the superiority of the offered PRNASCR scheme for the aimed task.

3.4. Binary- Vs. Multi-class evaluation

This subsection displays the COVID-19 identification results using our proposed PRNASCR for binary- and multi-class (see in Section 2.1), utilizing the 5-fold cross-validation. The detailed class-wise performance of our PRNASCR for both the binary- and multi-class is exhibited in the confusion metrics in Table 5 (left) and Table 5 (right), correspondingly.

The binary-classification results in Table 5 (left) show that among 254-NOR CT samples, correctly classified samples are 167 (67.75%), whereas only 87 (34.25%) samples are erroneously classified as NCP (false positive). It is also noteworthy that among 856-NCP samples, rightly classified samples are 848 (99.06%), whereas only 8 (0.94%) samples are wrongly classified as NOR (false negative). Again, the matrix in Table 5 (right) for multi-class recognition reveals the FN and FP for the COVID-19 identification, where number of wrongly classified CT images (type-I or type-II errors) are 66/256 (25.78%), 104/684 (15.20%), 39/125 (31.20%), and 16/47 (34.04%) respectively for the NOR-, MiNCP-,

Table 5
The confusion matrix for the COVID-19 identification on the MosMedData dataset from our proposed 3D-CNN network and preprocessing for the binary- (left) and multi- (right) class problems.

2-classes		Actual	
		NOR	NCP
Predict	NOR	167 65.75 %	8 0.94 %
	NCP	87 34.25 %	848 99.06 %

4-classes		Actual			
		NOR	MiNCP	MoNCP	SeNCP
Predict	NOR	188 74.02 %	67 9.80 %	3 2.40 %	2 4.26 %
	MiNCP	62 24.41 %	580 84.80 %	29 23.2 %	13 27.66 %
	MoNCP	3 1.18 %	22 3.22 %	86 68.80 %	1 2.13 %
	SeNCP	1 0.39 %	15 2.18 %	7 5.60 %	31 65.95 %

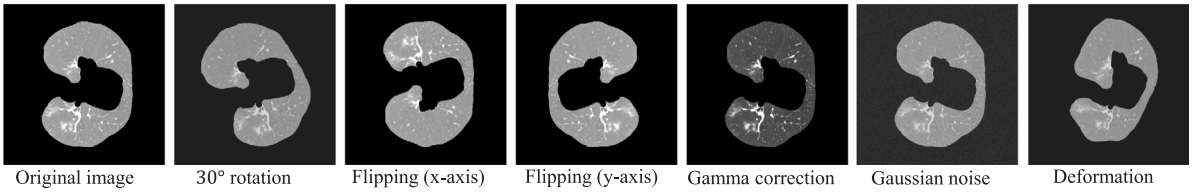

Fig. 8. Qualitative examples of augmentation results applied for automatic COVID-19 identification from the proposed framework.

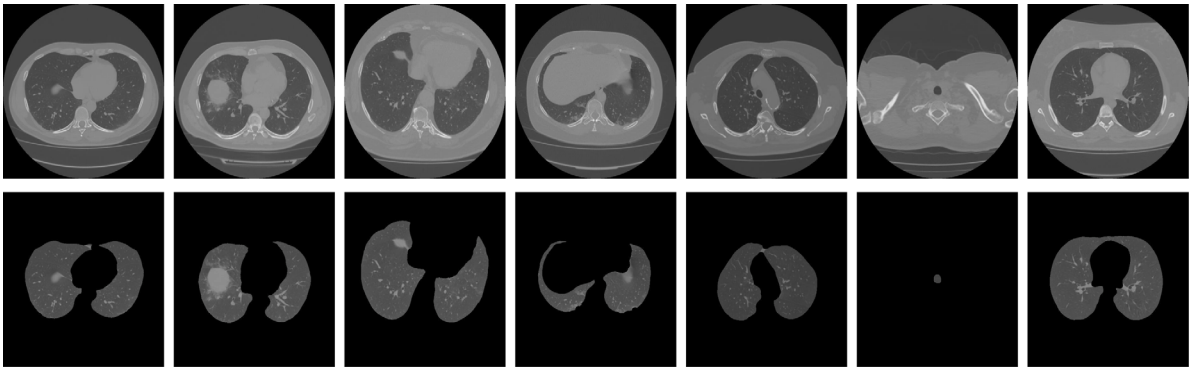

Fig. 9. Examples of lung segmentation results applying our unsupervised pipeline, as described in Section 2.2.

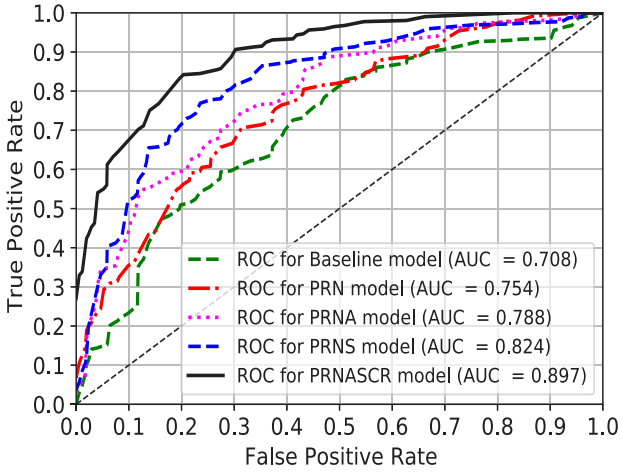

Fig. 10. The ROC curves for the employment of various preprocessing to our 3D network. Best view in the color figure. (For interpretation of the references to color in this figure legend, the reader is referred to the web version of this article.)

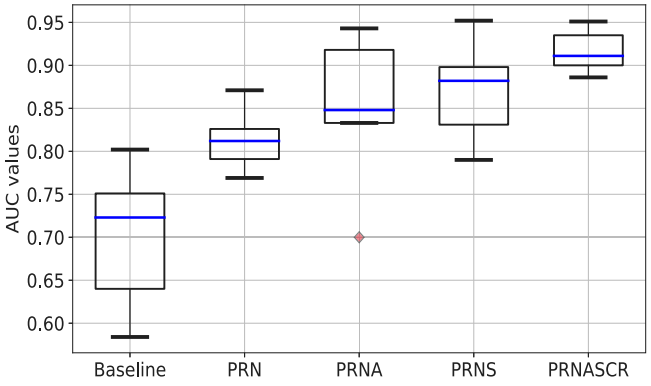

Fig. 11. Box and Whisker plot of the AUC values obtained from 5-fold cross-validation on different experiments in Table 4 for COVID-19 identification.

MoNCP-, and SeNCP-classes. Those binary- and multi-class results expose that the NOR-class performance has been improved by 8.27% margin with other constant experimental settings. The identification results for the severity prediction (MoNCP vs. SeNCP) confer tremendous success in our pipeline, where barely 5.60%-MoNCP and 2.13%-SeNCP samples are prognosticated as SeNCP- and MoNCP-classes, respectively (see in Table 5). Although overall macro-average AUC of the binary classification defeats the multi-class recognition (see in Fig. 12) by a margin of 2.1%, the later protocol has better class-balance results. The multi-class protocol also provides more minor inter-fold variation than the binary-class, as depicted in Fig. 12. However, our approach for the COVID-19 identification exhibits praiseworthy achievement with high AUC values with less inter-fold variation in both of the class protocols.

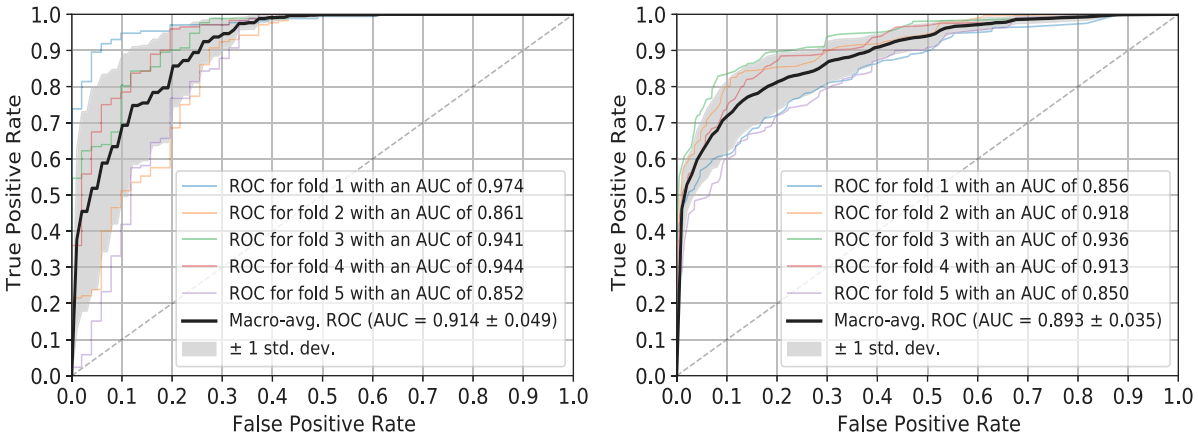

(a) ROC for binary-class (b) ROC for multi-class

Fig. 12. The ROC curves for the binary- and multi-class identification of COVID-19, applying 5-fold cross-validations. Best view in the color figure. (For interpretation of the references to color in this figure legend, the reader is referred to the web version of this article.)

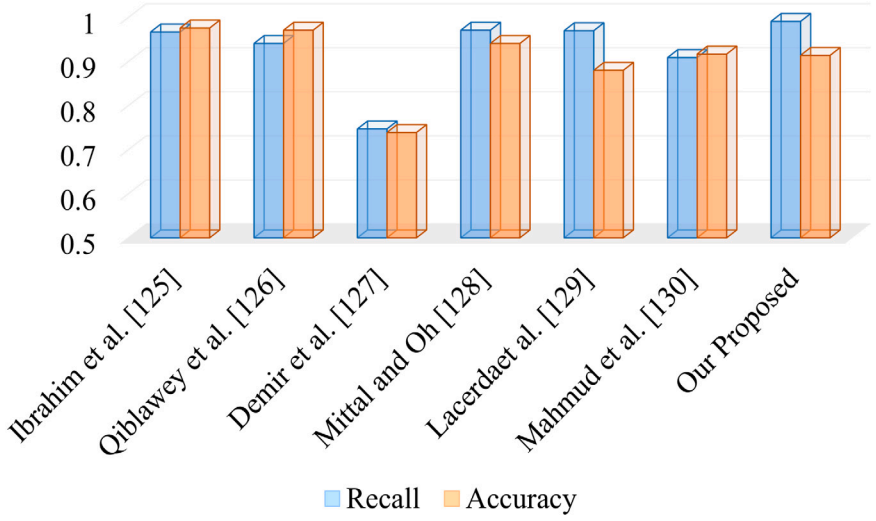

Fig. 13. Quantitative comparison of our proposed method with other techniques for the identical intended task and dataset using the Bar plots of recall and accuracy.

To compare our proposed framework with the existing works [125–130], we consider the articles, which are tested on the same MosMedData dataset. Fig. 13 exhibits a quantitative comparison of different methods for the same task and dataset, dispensing recall and accuracy. The comparative results in Fig. 13 point that the recommended framework achieves the highest recall of 0.991, delivering significantly less type-II error of COVID-19 identification. Although the accuracy of our system is less, it is still better than other methods of Ibrahim et al. [125], Qiblawey et al. [126], Demir et al. [127], Mittal and Oh [128], Lacerda et al. [129], Mahmud et al. [130] for medical diagnostic procedures because our system has significantly fewer false-negative rates with slightly higher false-positive rates. Additionally, most of the authors in [125–130] split data for training, validation, and testing without cross-validation. However, selecting test images in such a splitting cannot guarantee not choosing the most straightforward samples, which perhaps exhibited better accuracy from those articles.

4. Conclusion

During the current COVID-19 pandemic emergency, precise recognition with negligible false negative is essential to mitigate the permanent lung damage due to coronavirus. This article aimed to design an artificial screening system for automated COVID-19 identification. A progressively resized 3D-CNN classifier is recommended in this study, incorporating lung segmentation, image augmentations, and class-rebalancing. The experimental analysis confirms that the CNN classifier's training with the suitable smaller patches and progressively increasing the network size enhance the identification results. Furthermore, incorporating the lung segmentation empowers the classifier to learn salient and characteristic COVID-19 features rather than utilizing whole chest CT images, driving improved COVID-19 classification performance. Again, the augmentations and class-rebalancing result in improved COVID-19 identification with high class-balanced recognition, shielding the network from being biased to a particular overrepresented class. In the future, the proposed pipeline will be

employed in other volumetric medical imaging domains to validate its efficacy, versatility, and robustness. We also aim to deploy our trained model to a user-friendly web application for clinical utilization. The proposed system can be an excellent tool for clinicians to fight this deadly epidemic by the quicker and automated screening of the COVID-19.

CRediT authorship contribution statement

Md. Kamrul Hasan: Conceptualization, Methodology, Software, Formal analysis, Investigation, Visualization, Writing – review & editing, Supervision. **Md. Tasnim Jawad:** Software, Validation, Data curation, Writing – original draft. **Kazi Nasim Imtiaz Hasan:** Data curation, Writing – original draft. **Sajal Basak Partha:** Writing – original draft. **Md. Masum Al Masba:** Writing – original draft. **Shumit Saha:** Supervision. **Mohammad Ali Moni:** Writing – review & editing.

Declaration of competing interest

The authors declare that they have no known competing financial interests or personal relationships that could have appeared to influence the work reported in this paper.

Acknowledgments

The authors acknowledge the contributors of the publicly available MosMed dataset in this COVID-19 pandemic situation. The authors also acknowledge the Keras developer team for building the deep learning API.

References

[1] World Health Organization. Naming the coronavirus disease (COVID-19). 2020, https://bit.ly/3zQEqn5. [Accessed 16 July 2020].
[2] Wang D, Hu B, Hu C, Zhu F, Liu X, Zhang J, et al. Clinical characteristics of 138 hospitalized patients with 2019 novel coronavirus–infected pneumonia in Wuhan, China. JAMA 2020;323(11):1061–9.
[3] Chen N, Zhou M, Dong X, Qu J, Gong F, Han Y, et al. Epidemiological and clinical characteristics of 99 cases of 2019 novel coronavirus pneumonia in Wuhan, China: a descriptive study. Lancet 2020;395(10223):507–13.
[4] Li Q, Guan X, Wu P, Wang X, Zhou L, Tong Y, et al. Early transmission dynamics in Wuhan, China, of novel coronavirus–infected pneumonia. N Engl J Med 2020.
[5] Jain G, Mittal D, Thakur D, Mittal MK. A deep learning approach to detect Covid-19 coronavirus with X-Ray images. Biocybern Biomed Eng 2020;40(4):1391–405.
[6] Wu YC, Chen C-S, Chan YJ. The outbreak of COVID-19: An overview. J Chin Med Assoc 2020;83(3):217.
[7] Walker PG, Whittaker C, Watson OJ, Baguelin M, Winskill P, Hamlet A, et al. The impact of COVID-19 and strategies for mitigation and suppression in low-and middle-income countries. Science 2020.
[8] Wang W, Xu Y, Gao R, Lu R, Han K, Wu G, et al. Detection of SARS-CoV-2 in different types of clinical specimens. JAMA 2020;323(18):1843–4.
[9] Yang T, Wang YC, Shen CF, Cheng CM. Point-of-care RNA-based diagnostic device for COVID-19. 2020.
[10] NEWS AJ. Bangladesh scientists create $3 kit. Can it help detect COVID-19? . 2020, https://bit.ly/aj2020corona. [Accessed 14 July 2020].
[11] Huang C, Wang Y, Li X, Ren L, Zhao J, Hu Y, et al. Clinical features of patients infected with 2019 novel coronavirus in Wuhan, China. Lancet 2020;395(10223):497–506.
[12] Corman VM, Landt O, Kaiser M, Molenkamp R, Meijer A, Chu DK, et al. Detection of 2019 novel coronavirus (2019-nCoV) by real-time RT-PCR. Eurosurveillance 2020;25(3):2000045.
[13] Xu X, Jiang X, Ma C, Du P, Li X, Lv S, et al. A deep learning system to screen novel coronavirus disease 2019 pneumonia. Engineering 2020.
[14] Singh D, Kumar V, Kaur M. Classification of COVID-19 patients from chest CT images using multi-objective differential evolution–based convolutional neural networks. Eur J Clin Microbiol Infect Dis 2020;1–11.
[15] Lee EY, Ng MY, Khong PL. COVID-19 pneumonia: what has CT taught us? Lancet Infect Dis 2020;20(4):384–5.
[16] LeCun Y, Bengio Y, Hinton G. Deep learning. Nature 2015;521(7553):436–44.
[17] Krizhevsky A, Sutskever I, Hinton GE. Imagenet classification with deep convolutional neural networks. In: Advances in neural information processing systems. 2012, p. 1097–105.
[18] Edalatifar M, Tavakoli MB, Ghalambaz M, Setoudeh F. Using deep learning to learn physics of conduction heat transfer. J Therm Anal Calorim 2020;1–18.
[19] Edalatifar M, Tavakoli MB, Ghalambaz M, Setoudeh F. A dataset for conduction heat transer and deep learning. Mendeley Data 2020.
[20] Yıldırım Ö, Pławiak P, Tan RS, Acharya UR. Arrhythmia detection using deep convolutional neural network with long duration ECG signals. Comput Biol Med 2018;102:411–20.
[21] Hannun AY, Rajpurkar P, Haghpanahi M, Tison GH, Bourn C, Turakhia MP, et al. Cardiologist-level arrhythmia detection and classification in ambulatory electrocardiograms using a deep neural network. Nat Med 2019;25(1):65.
[22] Acharya UR, Oh SL, Hagiwara Y, Tan JH, Adam M, Gertych A, et al. A deep convolutional neural network model to classify heartbeats. Comput Biol Med 2017;89:389–96.
[23] Hasan MK, Dahal L, Samarakoon PN, Tushar FI, Martí R. DSNet: Automatic dermoscopic skin lesion segmentation. Comput Biol Med 2020;120:103738.
[24] Esteva A, Kuprel B, Novoa RA, Ko J, Swetter SM, Blau HM, et al. Dermatologist-level classification of skin cancer with deep neural networks. Nature 2017;542(7639):115–8.
[25] Codella NC, Nguyen QB, Pankanti S, Gutman DA, Helba B, Halpern AC, et al. Deep learning ensembles for melanoma recognition in dermoscopy images. IBM J Res Dev 2017;61(4/5):1–5.
[26] Dutta A, Hasan MK, Ahmad M. Skin lesion classification using convolutional neural network for melanoma recognition. 2020, medRxiv.
[27] Celik Y, Talo M, Yildirim O, Karabatak M, Acharya UR. Automated invasive ductal carcinoma detection based using deep transfer learning with whole-slide images. Pattern Recognit Lett 2020.
[28] Cruz-Roa A, Basavanhally A, González F, Gilmore H, Feldman M, Ganesan S, et al. Automatic detection of invasive ductal carcinoma in whole slide images with convolutional neural networks. In: Medical imaging 2014: digital pathology. vol. 9041, International Society for Optics and Photonics; 2014, 904103.
[29] Hasan M, Aleef TA, et al. Automatic mass detection in breast using deep convolutional neural network and svm classifier. 2019, arXiv:1907.04424.
[30] Talo M, Yildirim O, Baloglu UB, Aydin G, Acharya UR. Convolutional neural networks for multi-class brain disease detection using MRI images. Comput Med Imaging Graph 2019;78:101673.
[31] Tushar FI, Alyafi B, Hasan MK, Dahal L. Brain tissue segmentation using neuronet with different pre-processing techniques. In: 2019 joint 8th international conference on informatics, electronics & vision (ICIEV) and 2019 3rd international conference on imaging, vision & pattern recognition. IEEE; 2019, p. 223–7.
[32] Rajpurkar P, Irvin J, Zhu K, Yang B, Mehta H, Duan T, et al. Chexnet: Radiologist-level pneumonia detection on chest x-rays with deep learning. 2017, arXiv:1711.05225.
[33] Tan JH, Fujita H, Sivaprasad S, Bhandary SV, Rao AK, Chua KC, et al. Automated segmentation of exudates, haemorrhages, microaneurysms using single convolutional neural network. Inform Sci 2017;420:66–76.
[34] Hasan MK, Alam MA, Elahi MTE, Roy S, Martí R. DRNet: Segmentation and localization of optic disc and fovea from diabetic retinopathy image. Artif Intell Med 2020;102001.
[35] Gaál G, Maga B, Lukács A. Attention u-net based adversarial architectures for chest x-ray lung segmentation. 2020, arXiv:2003.10304.
[36] Sandler M, Howard A, Zhu M, Zhmoginov A, Chen L-C. Mobilenetv2: Inverted residuals and linear bottlenecks. In: Proceedings of the IEEE conference on computer vision and pattern recognition, 2018. p. 4510–20.
[37] Deng J, Dong W, Socher R, Li LJ, Li K, Fei Fei L. Imagenet: A large-scale hierarchical image database. In: 2009 IEEE conference on computer vision and pattern recognition. Ieee; 2009, p. 248–55.
[38] Apostolopoulos ID, Aznaouridis SI, Tzani MA. Extracting possibly representative COVID-19 Biomarkers from X-Ray images with Deep Learning approach and image data related to Pulmonary Diseases. J Med Biol Eng 2020;1.
[39] Abbas A, Abdelsamea MM, Gaber MM. Detrac: Transfer learning of class decomposed medical images in convolutional neural networks. IEEE Access 2020;8:74901–13.
[40] Abbas A, Abdelsamea MM, Gaber MM. Classification of COVID-19 in chest X-ray images using DeTraC deep convolutional neural network. 2020, arXiv:2003.13815.
[41] Ruder S. An overview of gradient descent optimization algorithms. 2016, arXiv:1609.04747.
[42] Simonyan K, Zisserman A. Very deep convolutional networks for large-scale image recognition. 2014, arXiv:1409.1556.
[43] Szegedy C, Liu W, Jia Y, Sermanet P, Reed S, Anguelov D, et al. Going deeper with convolutions. In: Proceedings of the IEEE conference on computer vision and pattern recognition, 2015. p. 1–9.
[44] Chollet F. Xception: Deep learning with depthwise separable convolutions. In: Proceedings of the IEEE conference on computer vision and pattern recognition, 2017. p. 1251–8.
[45] Szegedy C, Ioffe S, Vanhoucke V, Alemi A. Inception-v4, inception-resnet and the impact of residual connections on learning. 2016, arXiv:1602.07261.
[46] Howard AG, Zhu M, Chen B, Kalenichenko D, Wang W, Weyand T, et al. Mobilenets: Efficient convolutional neural networks for mobile vision applications. 2017, arXiv:1704.04861.

[47] Huang G, Liu Z, Van Der Maaten L, Weinberger KQ. Densely connected convolutional networks. In: Proceedings of the IEEE conference on computer vision and pattern recognition, 2017. p. 4700–8.

[48] Pham H, Guan MY, Zoph B, Le QV, Dean J. Efficient neural architecture search via parameter sharing. 2018, arXiv:1802.03268.

[49] Bergstra J, Bengio Y. Random search for hyper-parameter optimization. J Mach Learn Res 2012;13(1):281–305.

[50] Rajaraman S, Siegelman J, Alderson PO, Folio LS, Folio LR, Antani SK. Iteratively pruned deep learning ensembles for COVID-19 detection in chest X-rays. 2020, arXiv:2004.08379.

[51] Wu WJ, Lin SW, Moon WK. Combining support vector machine with genetic algorithm to classify ultrasound breast tumor images. Comput Med Imaging Graph 2012;36(8):627–33.

[52] Iandola FN, Han S, Moskewicz MW, Ashraf K, Dally WJ, Keutzer K. SqueezeNet: AlexNet-level accuracy with 50x fewer parameters and <0.5 MB model size. 2016, arXiv:1602.07360.

[53] Toğaçar M, Ergen B, Cömert Z. COVID-19 detection using deep learning models to exploit Social Mimic optimization and structured chest X-ray images using fuzzy color and stacking approaches. Comput Biol Med 2020;103805.

[54] Zhang X, Zhou X, Lin M, Sun J. Shufflenet: An extremely efficient convolutional neural network for mobile devices. In: Proceedings of the IEEE conference on computer vision and pattern recognition, 2018. p. 6848–56.

[55] Tan M, Le QV. Efficientnet: rethinking model scaling for convolutional neural networks. 2019, arXiv:1905.11946.

[56] Öksüz C, Urhan O, Güllü MK. Ensemble-CVDNet: A deep learning based end-to-end classification framework for COVID-19 detection using ensembles of networks. 2020, arXiv:2012.09132.

[57] Ozkaya U, Ozturk S, Barstugan M. Coronavirus (COVID-19) classification using deep features fusion and ranking technique. 2020, arXiv:2004.03698.

[58] Jaiswal A, Gianchandani N, Singh D, Kumar V, Kaur M. Classification of the COVID-19 infected patients using DenseNet201 based deep transfer learning. J Biomol Struct Dyn 2020;1–8.

[59] Angelov P, Almeida Soares E. Explainable-by-design approach for covid-19 classification via ct-scan. 2020, medRxiv.

[60] He K, Zhang X, Ren S, Sun J. Deep residual learning for image recognition. In: Proceedings of the IEEE conference on computer vision and pattern recognition, 2016. p. 770–8.

[61] Ko H, Chung H, Kang WS, Kim KW, Shin Y, Kang SJ, et al. COVID-19 pneumonia diagnosis using a simple 2D deep learning framework with a single chest CT image: model development and validation. J Med Internet Res 2020;22(6):e19569.

[62] Zhao J, Zhang Y, He X, Xie P. COVID-CT-dataset: a CT scan dataset about COVID-19. 2020, arXiv:2003.13865.

[63] Ronneberger O, Fischer P, Brox T. U-net: Convolutional networks for biomedical image segmentation. In: International conference on medical image computing and computer-assisted intervention. Springer; 2015, p. 234–41.

[64] Wang X, Deng X, Fu Q, Zhou Q, Feng J, Ma H, et al. A weakly-supervised framework for COVID-19 classification and lesion localization from chest CT. IEEE Trans Med Imaging 2020.

[65] Hasan M, Alam M, Elahi M, Toufick E, Roy S, Wahid SR, et al. CVR-Net: A deep convolutional neural network for coronavirus recognition from chest radiography images. 2020, arXiv:2007.11993.

[66] Alshazly H, Linse C, Barth E, Martinetz T. Explainable COVID-19 detection using chest CT scans and deep learning. 2020, arXiv:2011.05317.

[67] Pereira RM, Bertolini D, Teixeira LO, Silla Jr CN, Costa YM. COVID-19 identification in chest X-ray images on flat and hierarchical classification scenarios. Comput Methods Programs Biomed 2020;105532.

[68] Pathak Y, Shukla PK, Tiwari A, Stalin S, Singh S, Shukla PK. Deep transfer learning based classification model for COVID-19 disease. IRBM 2020.

[69] Waheed A, Goyal M, Gupta D, Khanna A, Al-Turjman F, Pinheiro PR. Covidgan: Data augmentation using auxiliary classifier gan for improved covid-19 detection. IEEE Access 2020;8:91916–23.

[70] Hasan M, Ahamed M, Ahmad M, Rashid M, et al. Prediction of epileptic seizure by analysing time series EEG signal using-NN classifier. Appl Bionics Biomech 2017;2017.

[71] Hasan MK, Alam MA, Das D, Hossain E, Hasan M. Diabetes prediction using ensembling of different machine learning classifiers. IEEE Access 2020;8:76516–31.

[72] Nour M, Cömert Z, Polat K. A novel medical diagnosis model for COVID-19 infection detection based on deep features and Bayesian optimization. Appl Soft Comput 2020;97:106580.

[73] Ouchicha C, Ammor O, Meknassi M. CVDNet: A novel deep learning architecture for detection of coronavirus (Covid-19) from chest x-ray images. Chaos Solitons Fractals 2020;140:110245.

[74] Hasan MK, Alam MA, Dahal L, Elahi MTE, Roy S, Wahid SR, et al. Challenges of deep learning methods for COVID-19 detection using public datasets. 2020, medRxiv.

[75] Wang SH, Govindaraj VV, Górriz JM, Zhang X, Zhang YD. Covid-19 classification by FGCNet with deep feature fusion from graph convolutional network and convolutional neural network. Inf Fusion 2020;67:208–29.

[76] Ozturk T, Talo M, Yildirim EA, Baloglu UB, Yildirim O, Acharya UR. Automated detection of COVID-19 cases using deep neural networks with X-ray images. Comput Biol Med 2020;103792.

[77] Ioffe S, Szegedy C. Batch normalization: Accelerating deep network training by reducing internal covariate shift. 2015, arXiv:1502.03167.

[78] Xu B, Wang N, Chen T, Li M. Empirical evaluation of rectified activations in convolutional network. 2015, arXiv:1505.00853.

[79] Khan AI, Shah JL, Bhat MM. Coronet: A deep neural network for detection and diagnosis of COVID-19 from chest x-ray images. Comput Methods Programs Biomed 2020;105581.

[80] Nayak SR, Nayak DR, Sinha U, Arora V, Pachori RB. Application of deep learning techniques for detection of COVID-19 cases using chest X-ray images: A comprehensive study. Biomed Signal Process Control 2020;64:102365.

[81] Zoph B, Vasudevan V, Shlens J, Le QV. Learning transferable architectures for scalable image recognition. In: Proceedings of the IEEE conference on computer vision and pattern recognition, 2018. p. 8697–710.

[82] Horry MJ, Chakraborty S, Paul M, Ulhaq A, Pradhan B, Saha M, et al. COVID-19 detection through transfer learning using multimodal imaging data. IEEE Access 2020;8:149808–24.

[83] He X, Wang S, Shi S, Chu X, Tang J, Liu X, et al. Benchmarking deep learning models and automated model design for COVID-19 detection with chest CT scans. 2020, medRxiv.

[84] Apostolopoulos ID, Mpesiana TA. Covid-19: automatic detection from x-ray images utilizing transfer learning with convolutional neural networks. Phys Eng Sci Med 2020;1.

[85] Sethy PK, Behera SK. Detection of coronavirus disease (covid-19) based on deep features. 2020, p. 2020, Preprints, 2020030300.

[86] Hemdan EED, Shouman MA, Karar ME. Covidx-net: A framework of deep learning classifiers to diagnose covid-19 in x-ray images. 2020, arXiv:2003.11055.

[87] Narin A, Kaya C, Pamuk Z. Automatic detection of coronavirus disease (covid-19) using x-ray images and deep convolutional neural networks. 2020, arXiv:2003.10849.

[88] Morozov S, Andreychenko A, Pavlov N, Vladzymyrskyy A, Ledikhova N, Gombolevskiy V, et al. MosMedData: Chest CT scans with COVID-19 related findings. 2020, medRxiv.

[89] Mahmud T, Alam M, Chowdhury S, Ali SN, Rahman MM, Fattah SA, et al. CovTANet: A hybrid tri-level attention based network for lesion segmentation, diagnosis, and severity prediction of COVID-19 chest CT scans. 2021, arXiv:2101.00691.

[90] Yip SS, Klanecek Z, Naganawa S, Kim J, Studen A, Rivetti L, et al. Performance and robustness of machine learning-based radiomic COVID-19 severity prediction. 2020, medRxiv.

[91] Jnawali K, Arbabshirani MR, Rao N, Patel AA. Deep 3D convolution neural network for CT brain hemorrhage classification. In: Medical imaging 2018: computer-aided diagnosis. vol. 10575, International Society for Optics and Photonics; 2018, p. 105751C.

[92] Singh SP, Wang L, Gupta S, Goli H, Padmanabhan P, Gulyás B. 3D deep learning on medical images: a review. Sensors 2020;20(18):5097.

[93] Huang X, Shan J, Vaidya V. Lung nodule detection in CT using 3D convolutional neural networks. In: 2017 IEEE 14th international symposium on biomedical imaging. IEEE; 2017, p. 379–83.

[94] Zhou X, Yamada K, Kojima T, Takayama R, Wang S, Zhou X, Hara T, Fujita H. Performance evaluation of 2D and 3D deep learning approaches for automatic segmentation of multiple organs on CT images. In: Medical imaging 2018: computer-aided diagnosis. vol. 10575, International Society for Optics and Photonics; 2018, p. 105752C.

[95] Hesamian MH, Jia W, He X, Kennedy P. Deep learning techniques for medical image segmentation: Achievements and challenges. J Digit Imaging 2019;32(4):582–96.

[96] Shojaii R, Alirezaie J, Babyn P. Automatic lung segmentation in CT images using watershed transform. In: IEEE international conference on image processing 2005. vol. 2, IEEE; 2005, II–1270.

[97] Wang J, Li F, Li Q. Automated segmentation of lungs with severe interstitial lung disease in CT. Med Phys 2009;36(10):4592–9.

[98] Ko JP, Betke M. Chest CT: automated nodule detection and assessment of change over time—preliminary experience. Radiology 2001;218(1):267–73.

[99] Cichocki A, Amari Si. Adaptive blind signal and image processing: learning algorithms and applications. John Wiley & Sons; 2002.

[100] Soille P, Vogt P. Morphological segmentation of binary patterns. Pattern Recognit Lett 2009;30(4):456–9.

[101] Hussain Z, Gimenez F, Yi D, Rubin D. Differential data augmentation techniques for medical imaging classification tasks. In: AMIA annual symposium proceedings. vol. 2017, American Medical Informatics Association; 2017, p. 979.

[102] Shorten C, Khoshgoftaar TM. A survey on image data augmentation for deep learning. J. Big Data 2019;6(1):60.

[103] Zhang K, Liu X, Shen J, Li Z, Sang Y, Wu X, et al. Clinically applicable AI system for accurate diagnosis, quantitative measurements, and prognosis of covid-19 pneumonia using computed tomography. Cell 2020.

[104] Deng L, Liu Y. Deep learning in natural language processing. Springer; 2018.

[105] Cai L, Gao J, Zhao D. A review of the application of deep learning in medical image classification and segmentation. Ann Transl Med 2020;8(11).
[106] Fu Y, Lei Y, Wang T, Curran WJ, Liu T, Yang X. Deep learning in medical image registration: a review. Phys Med Biol 2020;65(20):20TR01.
[107] Ji Y, Zhang H, Zhang Z, Liu M. CNN-based encoder-decoder networks for salient object detection: A comprehensive review and recent advances. Inform Sci 2021;546:835–57.
[108] Dhruv P, Naskar S. Image classification using convolutional neural network (CNN) and recurrent neural network (RNN): A review. Mach Learn Inf Process 2020;367–81.
[109] Long Y, Gong Y, Xiao Z, Liu Q. Accurate object localization in remote sensing images based on convolutional neural networks. IEEE Trans Geosci Remote Sens 2017;55(5):2486–98. http://dx.doi.org/10.1109/TGRS.2016.2645610.
[110] Ozsahin I, Sekeroglu B, Musa MS, Mustapha MT, Uzun Ozsahin D. Review on diagnosis of COVID-19 from chest CT images using artificial intelligence. Comput Math Methods Med 2020;2020.
[111] Bhattacharya S, Maddikunta PKR, Pham QV, Gadekallu TR, Chowdhary CL, Alazab M, et al. Deep learning and medical image processing for coronavirus (COVID-19) pandemic: A survey. Sustainable Cities Soc 2021;65:102589.
[112] Sarvamangala D, Kulkarni RV. Convolutional neural networks in medical image understanding: a survey. Evol Intell 2021;1–22.
[113] Litjens G, Kooi T, Bejnordi BE, Setio AAA, Ciompi F, Ghafoorian M, et al. A survey on deep learning in medical image analysis. Med Image Anal 2017;42:60–88.
[114] Lu H, Wang H, Zhang Q, Yoon SW, Won D. A 3D convolutional neural network for volumetric image semantic segmentation. Procedia Manuf 2019;39:422–8.
[115] Lin M, Chen Q, Yan S. Network in network. 2013, arXiv:1312.4400.
[116] Srivastava N, Hinton G, Krizhevsky A, Sutskever I, Salakhutdinov R. Dropout: a simple way to prevent neural networks from overfitting. J Mach Learn Res 2014;15(1):1929–58.
[117] Yadav SS, Jadhav SM. Deep convolutional neural network based medical image classification for disease diagnosis. J. Big Data 2019;6(1):1–18.
[118] Jiménez-Sánchez A, Albarqouni S, Mateus D. Capsule networks against medical imaging data challenges. In: Intravascular imaging and computer assisted stenting and large-scale annotation of biomedical data and expert label synthesis. Springer; 2018, p. 150–60.
[119] Wang X, Peng Y, Lu L, Lu Z, Summers RM. Tienet: Text-image embedding network for common thorax disease classification and reporting in chest x-rays. In: Proceedings of the IEEE conference on computer vision and pattern recognition, 2018. p. 9049–58.
[120] Cheplygina V, de Bruijne M, Pluim JP. Not-so-supervised: a survey of semi-supervised, multi-instance, and transfer learning in medical image analysis. Med Image Anal 2019;54:280–96.
[121] Arani E, Marzban S, Pata A, Zonooz B. Rgpnet: A real-time general purpose semantic segmentation. In: Proceedings of the IEEE/CVF winter conference on applications of computer vision, 2021. p. 3009–18.
[122] Kingma DP, Ba J. Adam: A method for stochastic optimization. 2014, arXiv:1412.6980.
[123] Reddi SJ, Kale S, Kumar S. On the convergence of adam and beyond. 2019, arXiv:1904.09237.
[124] Géron A. Hands-on machine learning with scikit-learn, keras, and TensorFlow: concepts, tools, and techniques to build intelligent systems. O'Reilly Media; 2019.
[125] Ibrahim MR, Youssef SM, Fathalla KM. Abnormality detection and intelligent severity assessment of human chest computed tomography scans using deep learning: a case study on SARS-COV-2 assessment. J Ambient Intell Humaniz Comput 2021;1–24.
[126] Qiblawey Y, Tahir A, Chowdhury ME, Khandakar A, Kiranyaz S, Rahman T, et al. Detection and severity classification of COVID-19 in CT images using deep learning. Diagnostics 2021;11(5):893.
[127] Demir U, Irmakci I, Keles E, Topcu A, Xu Z, Spampinato C, et al. Information bottleneck attribution for visual explanations of diagnosis and prognosis. 2021, arXiv:2104.02869.
[128] Mittal B, Oh J. CoviNet: Covid-19 diagnosis using machine learning analyses for computerized tomography images. In: Thirteenth international conference on digital image processing. vol. 11878, International Society for Optics and Photonics; 2021, 1187816.
[129] Lacerda P, Barros B, Albuquerque C, Conci A. Hyperparameter optimization for COVID-19 pneumonia diagnosis based on chest CT. Sensors 2021;21(6):2174.
[130] Mahmud T, Alam MJ, Chowdhury S, Ali SN, Rahman MM, Fattah SA, et al. CovTANet: A hybrid tri-level attention-based network for lesion segmentation, diagnosis, and severity prediction of COVID-19 chest CT scans. IEEE Trans Ind Inf 2020;17(9):6489–98.